MIT Open Access Articles

Effects of Defect Development During Displacive Austenite Reversion on Strain Hardening and Formability

Massachusetts Institute of Technology

Effects of Defect Development During Displacive Austenite Reversion on Strain Hardening and Formability

Effects of defect development during displacive austenite reversion on strain hardening and formability

Menglei Jiang[1], Jiyun Kang[1], Charles Arthur Hirst[2], and Cemal Cem Taşan[*1].

[1]Department of Materials Science and Engineering, MIT, 77 Massachusetts Ave., Cambridge, MA 02139, USA

[2]Department of Nuclear Engineering, MIT, 77 Massachusetts Ave., Cambridge, MA 02139, USA

[*]Corresponding author: Cemal Cem Taşan (tasan@mit.edu)

Abstract

Martensite that is mechanically induced from metastable austenite can be reversed to austenite upon annealing. The reversion transformation can be either diffusive or displacive, and the defect substructure development, in either case, has mechanical consequences. Here, to better understand the effects of microstructure development during displacive phase transformations, we focus on the influence of the initial plastic deformation on the austenite reversion ($\alpha' \rightarrow \gamma$) in a transformation-induced plasticity-maraging steel. The phase transformation kinetics and the developing defect structure within the reversed γ phase are characterized by carrying out differential scanning calorimetry measurements, electron backscatter diffraction, and electron channeling contrast imaging analyses. The resulting mechanical behavior is investigated by uniaxial and biaxial tension experiments. These investigations demonstrate that the defect development during sequential deformation-annealing treatments can help increase the overall strain hardening capacity of the alloy, which in turn increases the accumulative uniform elongation, and the formability. While the necking can be progressively delayed to higher strain levels following such treatments, the local fracture strain apparently cannot be, due to damage accumulation.

Keywords

Metastability; steel; TRIP-maraging; damage; strain path

1. Introduction

Reverted austenite can be transformed from parent martensite through diffusive, or displacive (martensitic) transformations [1–4]. In the former case, the austenite is typically stabilized by the diffusion of one or more austenite stabilizer alloying element(s) to existing lath martensitic boundaries [3]. The kinetics of this transformation thus depend on diffusion kinetics and martensite dislocation density [5,6]. For example, higher austenite reversion rates are observed

1

when parent martensite has a higher dislocation density [5]. The austenite grains resulting from such diffusive transformations have low crystallographic defect density [3,7], regardless of the starting state of the parent phase. In displacive transformations [8], which typically occur at high heating rates [9,10], prior dislocations can create opposing kinetic effects. Dislocations can provide nucleation sites for austenite formation [11], but they may also impose stress fields, which can hinder austenite growth [12]. Importantly, the austenite grains resulting from such displacive reverse transformations have specific crystallographic orientations (arising from the crystallographic orientation relationships with the parent phase [2]) and high defect density [6,11].

The density and character of the defects present in reversed austenite, such as dislocations [13,14], precipitates [15], twins [16], or micro-cracks [17], can create differences in the mechanical stability of austenite, and in the overall mechanical properties of the corresponding alloys. In this regard, dislocation characteristics have an especially significant role. For example, it was reported in a medium Mn steel [13], where warm rolling is applied to introduce extra dislocations in reversed austenite, that dislocations stabilize the austenite phase and increase the critical transformation stress/strain and the yield strength. Moreover, mechanically induced phase transformation rate is maintained or even decreased, which allows the warm-rolled steel to show similar work hardening rate and ductility as the non-rolled steel. In another work on stainless steel [18], the cyclic thermal-induced $\gamma \rightarrow \alpha$ phase transformation introduces austenite memory effect [2]. The high dislocation density from phase transformation also increases the yield stress. However, in contrast to the previously mentioned work, the mechanically induced phase transformation rate significantly increases, which provides a higher work hardening rate. We have also demonstrated

2

earlier, focusing on a transformation-induced plasticity (TRIP)-assisted high entropy alloy (HEA), that cyclic phase transformations introduce geometrically necessary dislocations (GNDs) in austenite. The increased GND density help nucleate secondary HCP-martensite variants, which in turn increases work hardening rates [19]. We have also showed that a near full microstructure reversion can be achieved in TRIP-assisted maraging steel following a deformation-annealing process. The recovery of dislocation density enables the material to reproduce the same stress-strain curve as original state [20].

It is thus clear that the defect density and character introduced during displacive austenite reversion transformations are engineering parameters that should be considered in the design and processing of TRIP-assisted steels. To this end, this present work focuses on the utilization of the defect structure from displacive austenite reversion transformations to alter the mechanically induced phase transformation of austenite and explore the possibility of improving the resulting strain hardening capacity and the resulting strength-ductility combinations. To achieve this, we systematically investigate austenite reversion in TRIP-maraging steel, which was previously studied to better understand the mechanisms of mechanically induced martensitic transformation and twinning [16,21], damage-resistance [17], and austenite reversion [5,20].

2. Experiments

The investigated TRIP-maraging steel has the nominal composition of Fe-9Mn-3Ni-1.4Al-0.01C (wt.%) [21]. The ingot was cast and hot-rolled at 1100 °C and homogenized at 1100 °C for 1 hour with a water quench. Then samples are cold rolled at room temperature with ~70% thickness reduction (S_{CR}) and then annealed at 600 °C for one hour ($S_{original}$) [21]. The kinetics of the back

3

transformation is studied via differential scanning calorimetry (DSC) and isothermal annealing. For the DSC tests, the $S_{original}$ samples are cold-rolled at room temperature (~30% thickness reduction). We refer to these as $S_{deformed}$. Thus, $S_{deformed}$ samples consist of a martensitic matrix and deformation-induced martensite. Then the $S_{deformed}$ samples are cut into 5 mm disks with a wire electrical discharge machine (wire-EDM) and surface polished with 40 nm colloidal silica suspension (OPS) as the final step. The samples are heated up from room temperature to 1400 ℃ with five heating rates, 5 K/min, 10 K/min, 20 K/min, 30 K/min, and 50 K/min. The background of DSC is fitted with a spline curve for both the start segment and the end segment. Then the peak of interest is subtracted from the background baseline, fitted with a Gaussian model to locate the peak maximum temperature and to identify transformation start- and end-points [22]. Isothermal annealing tests are performed on samples ($S_{deformed}$) with different strain levels (i.e. either due to rolling or uniaxial tension). The isothermal treatment temperature is 600 ℃ for different durations (5 min, 15 min, and 60 min). For these treatments, samples are directly placed into a pre-heated 600 ℃ furnace. The furnace reaches equilibrium within 5 minutes after the sample is placed. After the treatment, samples are water quenched to room temperature ($S_{annealed}$).

Mechanical tests of $S_{original}$ and $S_{annealed}$ are carried out using a Gatan MTEST2000 Uniaxial Testing Stage with a 2 KN load cell at ~10^{-4} strain rate. Samples are cut using wire-EDM to a dog-bone shape, with a 5 mm gauge length and a 1.5 mm width. A homemade punch setup [23] is used to carry out biaxial tension tests, where the upper hole has a diameter of 25.4 mm, and the punch has a diameter of 12.7 mm. All the samples are kept the same thickness of ~ 1.5 mm after surface OPS polishing. Digital image correlation (DIC) is used to carry out strain measurements

4

using GOM Correlate and Vic-3D software. Different numbers of cycles of deformation-annealing processes (i.e. uniform deformation followed by isothermal annealing) are carried out. The accumulative ductility is also measured based on the DIC method.

The microstructures of samples at original ($S_{original}$), deformed ($S_{deformed}$), and annealed ($S_{annealed}$) states are characterized using TESCAN MIRA3 scanning electron microscope (SEM) equipped with an electron-backscattered diffraction (EBSD) camera, low-energy backscattered-electron (LE-BSE) detector, and energy dispersive spectrometer (EDS). EBSD measurements are carried out with an acceleration voltage of 15 kV with a step size of 40 nm. EDS measurements are also carried out with an acceleration voltage of 15 kV. The electron channeling contrast imaging (ECCI) [24] is performed with an acceleration voltage of 30 kV, using the LE-BSE detector. Damage evaluation in the tested materials is identified by image analysis, employing DIC data to identify local strain values, and the ImageJ analysis of secondary electron (SE) images [25] to quantify corresponding damage fractions.

3. Results

3.1. Original microstructure

The original microstructure is formed by an intercritical annealing from cold-rolled martensite [5]. Fig. 1a shows the EBSD phase map of the cold-rolled sample (S_{CR}). The S_{CR} has a fully martensitic structure (blue color in Fig. 1a) with a high boundary density. The missing data points correspond to the most severely deformed regions, as confirmed by ECCI. After annealing (Fig. 1b), equiaxed metastable austenite grains [5] (orange color) form at martensite boundaries,

5

to constitute 33% of the microstructure (average grain size 0.2 ± 0.1 μm from EBSD scan). Fig. $1b_2$ shows the magnified BSE image of the box region in Fig. $1b_1$. The EDS line scan (Fig. $1b_3$) across α'- γ grain boundaries shows the mass percent changes of alloying elements across α'- γ phase, which confirms Mn enrichment within the austenite phase (γ) [21]. Other elements (Al and Ni) show no preferential segregation, within the resolution limitations of SEM-EDS.
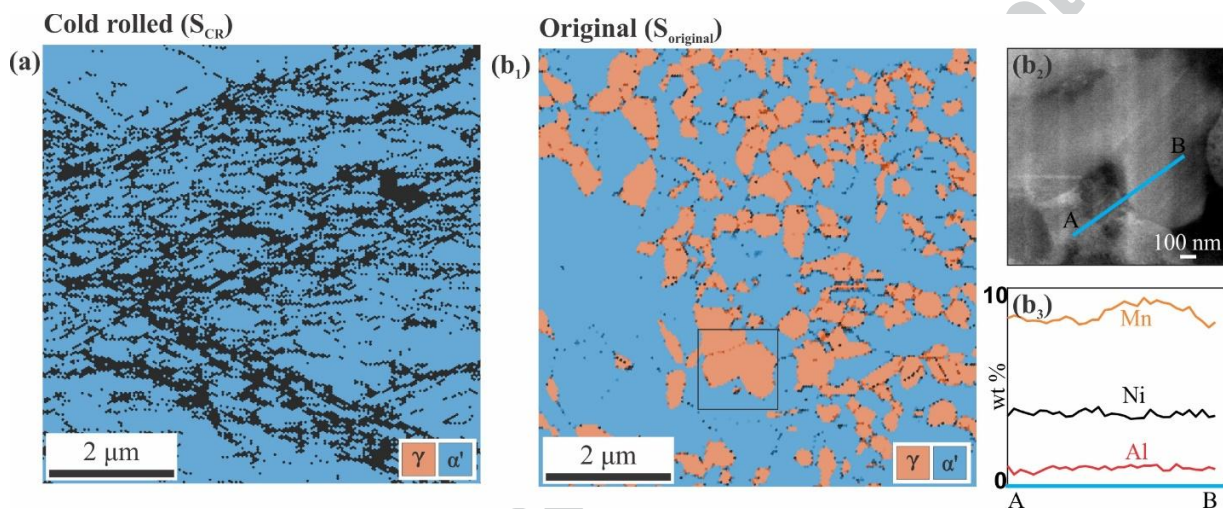

Figure 1. EBSD phase maps of **(a)** S_{CR} and **(b_1)** $S_{original}$, where the orange region represents the austenite phase, the blue region represents the martensite phase, and the black region represents the region with confident index lower than 0.1; and **(b_2)** BSE image of $S_{original}$ with (b_3) EDS line scan with A, B as the start- and end-points.

3.2. Austenite reversion kinetics

The austenite reversion transformation can be either diffusive or displacive [1–3,9]. To maximize the microstructure changes from displacive transformation, analyzing austenite reversion kinetics is necessary. For this purpose, DSC tests are carried out (Fig. 2a-c). After background subtraction (Fig. 2a), three peaks are identified: peak1 at ~ 500 °C, peak2 at ~ 600 °C, and peak3 at ~720 °C. To clearly show the peak location changes as a function of heating rate, the time-temperature-transformation diagram is plotted in Fig. 2b. Peak1 location is shifted to higher

6

temperatures with increasing heating rate, which is characteristic of a diffusion-controlled process [26–28]. Peak2 does not noticeably shift as the heating rate increases, as can be seen in the temperature-heating rate diagram (Fig. 2c). The transformation starts at ~ 500 °C and ends at ~760 °C, and both transformations' start and end temperatures are approximately constant (with ~30 K variation) as heating rate increases from 5 K/min to 50 K/min. Peak3 appears at relatively higher temperatures and shows a shift to higher temperature as the heating rate increases. Also considering previous Calphad calculations which revealed that the α-γ two-phase region is between 400°C and 700°C [29], we identify that peak1 represents a diffusive α'→γ transformation, peak2 represents a displacive α'→γ transformation, and peak3 represents the recovery peak of the γ phase [28]. At heating rates greater than 20 K/min, peak1 disappears or becomes merged with peak2, suggesting that displacive transformation is the dominant transformation mechanism at a high heating rate.

The isothermal annealing tests of $S_{deformed}$ (Fig. 2d) further confirm the reversion temperature and kinetics. For the diffusive mechanism, the transformation volume fraction is a function of the annealing time [28,30]. The volume fraction during displacive transformation, on the other hand, can be time-independent [31]. Here, the annealing temperature is chosen to be 600 °C, where the $S_{annealed}$ and $S_{original}$ would have similar thermodynamic equilibrium states. The austenite fraction shows a fast increase in the first 5 minutes (around 20% of austenite reversed), and then it slows down and reaches the equilibrium fraction after 1-hour annealing (total austenite fraction reaches ~32%). This phenomenon is distinct from segregation induced reverted austenite that we worked on [21]. This isothermal annealing treatment is shown (as a solid red line) in Fig. 2b, which

7

matches the transformation process as discussed: the $S_{deformed}$ sample first goes through a displacive α'→γ transformation. However, the reversion by displacive transformation is not complete (transformation finish temperature ~760 °C from Fig. 2c); thus a diffusive transformation follows [1].
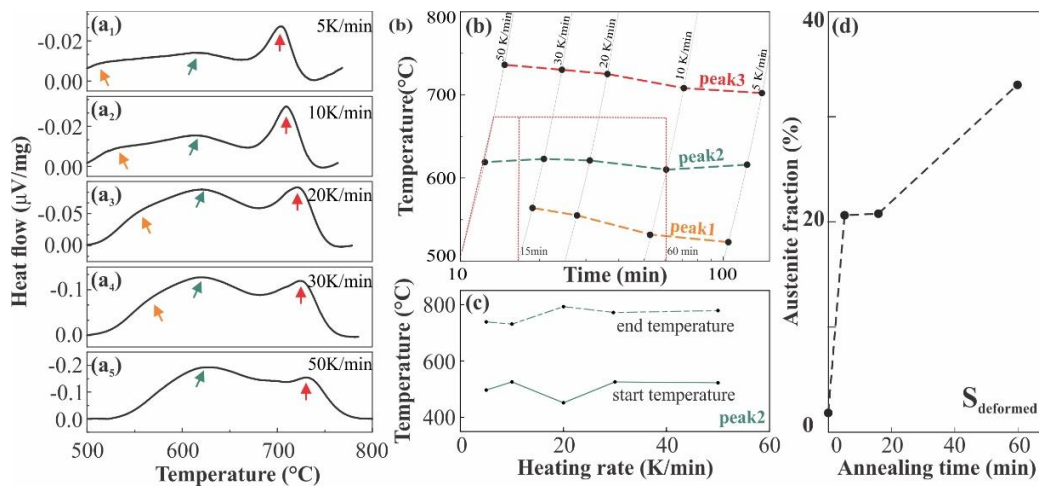

Figure 2. DSC analyses of $S_{deformed}$ (cold roll ~30%), with heating rates **(a₁)** 5 K/min, **(a₂)** 10 K/min, **(a₃)** 20 K/min, **(a₄)** 30 K/min and **(a₅)** 50K/min after background subtraction, where the endothermic goes up (negative). The peak1, peak2, and peak3 is highlighted by arrows. **(b)** time-temperature-transformation graph of peak1, peak2, and peak3, where the peak maximum temperature is shown; **(c)** peak2 transformation start and end temperature as function of heating rate; **(d)** the austenite fraction changes as function of time during isothermal annealing at 600 °C of $S_{deformed}$ (pre-strain ~60%) measured from multiple EBSD phase maps.

3.3. Microstructure evolution during displacive reversion

The DSC results suggest that the austenite reversion upon 15 min annealing takes place via displacive transformation (Fig. 2). However, confirmation of shear reversion requires microscopic investigations. Here, ECCI analysis coupled with EBSD mapping is employed to further investigate microstructure evolution during austenite reversion upon 15 min annealing at 600 °C, to demonstrate (focusing on three representative grains in Fig. 3) the process of shear transformation to austenite, followed by recrystallization. Note that, to characterize reversed

8

austenite grains but not plastically deformed austenite, a severe deformation step is applied (reaching ~60% local strains) prior to annealing, so that the austenite content at the deformed stage is less than 1% (Fig. 3).

Prior to the discussion of these results, however, it is useful to remember some of the characteristics of displacive transformations. In such transformations, austenite maintains a Kurdjumov–Sachs (K-S) orientation relationship with respect to the martensite phase to decrease interface energy during nucleation, where $(111)_\gamma$ // $(1\text{-}10)_\alpha$ and $[\text{-}110]_\gamma$ // $[\text{-}111]_\alpha$, within 5° variations [2,32]. Most reversed austenite grains develop acicular shapes to maintain special K-S relationships [11]. Given that no diffusion takes place during transformation, the austenite inherits the dislocation substructure from the parent martensite phase [8,11]. The volume change and grain rotation during displacive reversion creates heterogeneous stress fields, and, in turn, defect density distributions, in the neighboring martensite [8]. Diffusive transformation, on the other hand, shows different characteristics. Martensite boundary, which has high interface energy, is preferred for austenite nucleation [5]. The K-S relationship is not necessarily maintained [33]. Moreover, the austenite formed typically has low defect density and granular shape [5].
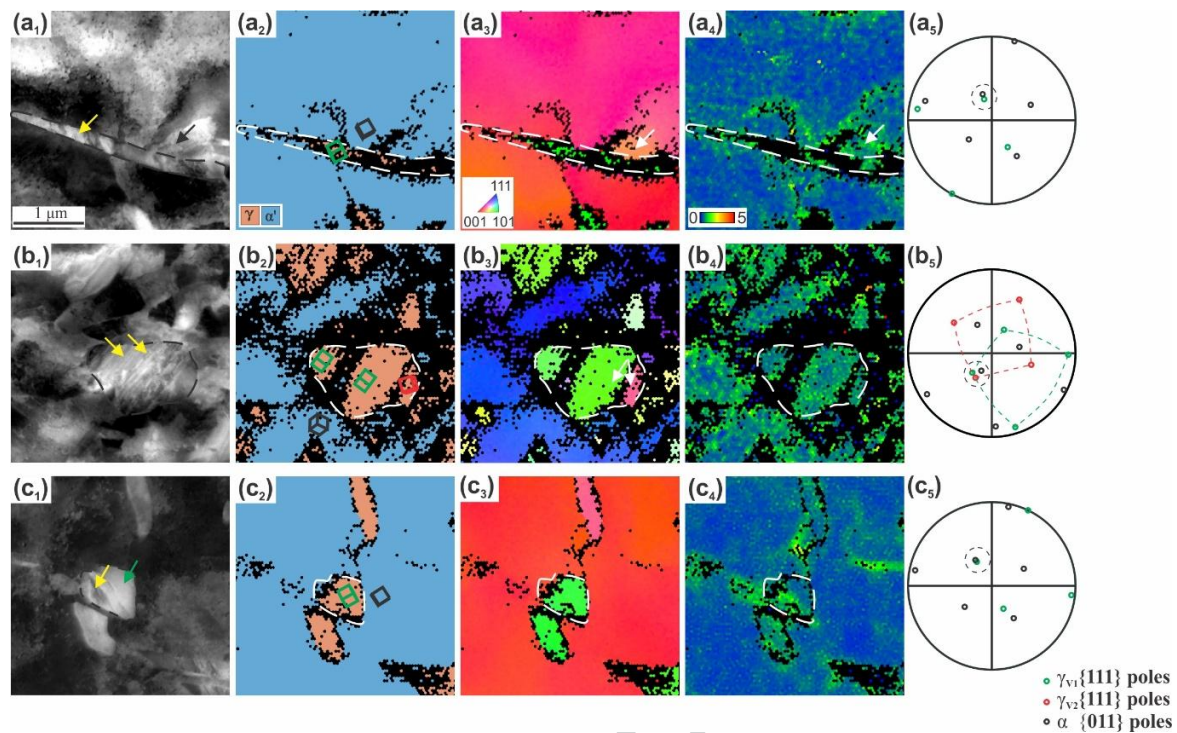
9

Figure 3. (a-c) Microstructure of reversed austenite grains in $S_{annealed}$ with (**1**) ECCI images, (**2**) EBSD phase map, (**3**) kernel average misorientation (KAM) map, (**4**) inverse pole figure (IPF) map, and (**5**) pole figure. The dashed line in 1-4 map shows the grain boundary of the austenite grain.

In Fig. $3a_1$, we focus on the lath shaped austenite grain in the middle of the image, fully surrounded within a single martensitic block, within which the maximum misorientation remains lower than ~3° (a_3). Previous ECCI studies on BSE contrast variations [34] suggest that the features observed in this austenite grain (e.g., see yellow arrows in a_1) are due to the presence of stacking faults. The same feature is also observed in other austenite grains (e.g. yellow arrow in b_1, c_1). In the corresponding EBSD phase map (a_2), several regions of the austenite grain are not indexed, and the indexed pixels have relatively high kernel average misorientation (KAM) values (a_4). Both can arise again due to high crystallographic defect density. The pole figure (a_5, see the dashed circle) demonstrates the parallelism between martensitic {011} planes and

10

austenitic {111} planes, i.e., the presence of the K-S relationship among the two phases. As fluctuations in BSE contrast, the orientation information in the inverse pole figures, and the local KAM values jointly suggest (see, e.g. the black arrows in a_1, and white arrows in a_3, a_4) the surrounding martensite shows local variations in orientation, and likely also in stress distributions. All these features match the characteristics of shear reversion highlighted previously.

The austenitic zones in Fig. 3b and Fig. 3c show different characteristics compared to the grain in Fig. 3a. First, both austenite grains exhibit granular shapes. The development of granular morphology suggests that reversion from martensite to austenite is complete and reversed austenite inherits the martensite boundaries [9]. Focusing on the region circled by a dashed line in Fig. 3b, two orientations can be observed (b_3, white arrow) suggesting the nucleation of two different variants, whereas in Fig. $3c_3$ a single variant austenite has transformed from martensite. The corresponding pole figure (b_5) shows that both austenite variants (green and red dots) follow the K-S relationship with the martensite matrix (black dots). Similarly, the pole figure in Fig. $3c_5$ also confirms the K-S relationship between the austenite and its surrounding martensite. Again, in both cases, in the chosen channeling condition, some variations in the BSE contrast are observed. For example, in Fig. $3b_1$ in the grain on the left stacking fault contrast is observed (yellow arrow), but not in the grain on the right (green arrow). A similar difference is seen in the BSE map in Fig. $3c_1$ comparing the regions marked with yellow and black arrows. The K-S relationship and the high defect density of the resulting austenite grains match the displacive transformation characteristics. One difference among these two regions is the observed KAM

11

values. While the austenitic grains in Fig. $3b_4$ both exhibit approximately the same average KAM values (which is as high as the KAM of the surrounding martensite), in Fig. $3c_4$ the two sides show large differences in the average KAM values (see yellow and green arrows in Fig. $3c_1$ and the corresponding region in Fig. $3c_4$). This difference suggests that the two regions in Fig. 3b and Fig. 3c are at different stages of the recovery process (low defect density is a sign of recovery [1]), following the completion of the martensitic reversion of the austenite.

3.4. Pre-strain effects on displacive reversion

As the isothermal annealing experiments demonstrate, when the annealing temperature is kept at 600 °C, a full reversion of austenite is not achievable by only displacive phase transformation. To maintain the austenite fraction of $S_{annealed}$ the same as $S_{original}$ (which is critical to be able to make systematic comparisons), while maximizing the effect of displacive transformations, it is required to carry out a systematic study of pre-strain effects. For this purpose, a TRIP-maraging steel sample is fractured by straining in uniaxial tension and then isothermally annealed for 15 minutes at 600 °C. The evolution of the austenite fraction is investigated by carrying out EBSD measurements, as shown by phase maps in Fig. 4, which are quantitatively compared in Fig. 5a. When deformed in uniaxial tension, the $S_{original}$ exhibits a yield strength of 950 MPa, an ultimate tensile strength of 1000 MPa, a uniform elongation of 14%, and a total elongation-to-failure of 28% (Fig. 5c). The austenite fraction changes from 36% to 0% as local engineering strain increases from 2% to 58% (Fig. 4a). There is a large decrease in austenite fraction between local strain 2% to 12% (uniform elongation), where two-thirds of austenite transforms to martensite (Fig. $4a_{1-2}$). Upon quantifying the kernel average misorientation (KAM) in austenite grains, an

12

increase in average KAM is observed (Fig. 5b), implying an increase in the geometrically necessary dislocation density in austenite grains [35]. The austenite grain size is also quantified from the EBSD phase map (Fig. 5b). A 25% decrease in austenite grain size is observed after uniform deformation, implying a higher transformation tendency for larger austenite grains [36,37]. A decrease of the austenite transformation rate is observed during post-necking deformation, showing mechanical stabilization of austenite [38] (Fig. 5a). The remaining austenite exhibits a further increase of average KAM values and a decrease of grain size under post-necking deformation. The error bar in Fig. 5b, Fig. 5c is obtained by calculating the standard deviation of austenite grains within EBSD maps (Fig. 4). The standard deviation means that the austenite characteristic is not uniform. From previous studies of this material [5], the austenite shows a spectral distribution of stability. Upon plastic deformation, the non-homogeneous transformation widens the deviation of the grain size and average KAM. When the strain further increases, the majority of austenite grains transform to martensite. The number of austenite grains decreases, and only stable austenite grains remain. Thus, the deviation decreases.
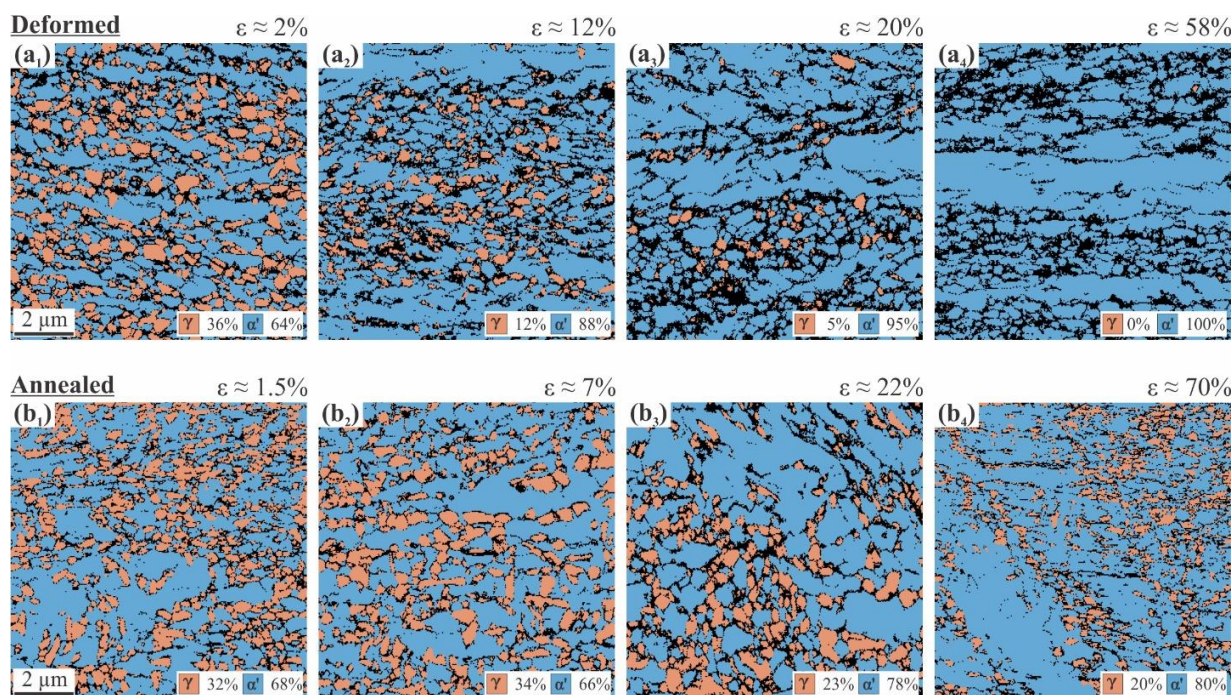
13

Figure 4. Post-mortem analyses of microstructure evolution during straining, and upon the follow-up annealing treatments: EBSD phase maps of **(a)** $S_{deformed}$ and **(b)** $S_{annealed}$ at **($_{1-4}$)** different local strain levels.

The comparison of $S_{annealed}$ (Fig. 4b) with $S_{deformed}$ (Fig. 4a) reveals a decrease in the initial austenite fraction, but this is within the standard deviation of the original austenite fraction (Fig. 5a orange region). At low pre-strain levels of 1.5% to 7% (within uniform elongation range, where local strain equals global strain), the displacive austenite reversion takes place according to the DSC results (Fig. 2), and the austenite phase fraction goes back to 34%, which is approximately equal to the austenite fraction in $S_{annealed}$ without pre-strain (Fig. 4b$_1$). From the EBSD phase map, the austenite grains are homogeneously distributed and equiaxed (Fig. 4b$_2$), and have approximately the same grain size and average KAM as $S_{original}$ (Fig. 5b, Fig. 5c). At 70% pre-strain, where all austenite transforms to martensite, the austenite volume fraction returns to 20% after annealing. The reversed austenite has a higher GND density (Fig. 5b), a smaller grain

14

size (Fig. 5c), and more acicular shapes (in Fig. $4b_4$ the austenite aspect ratio is 0.46 ± 0.14, while in $4a_1$ it is 0.51 ± 0.12).

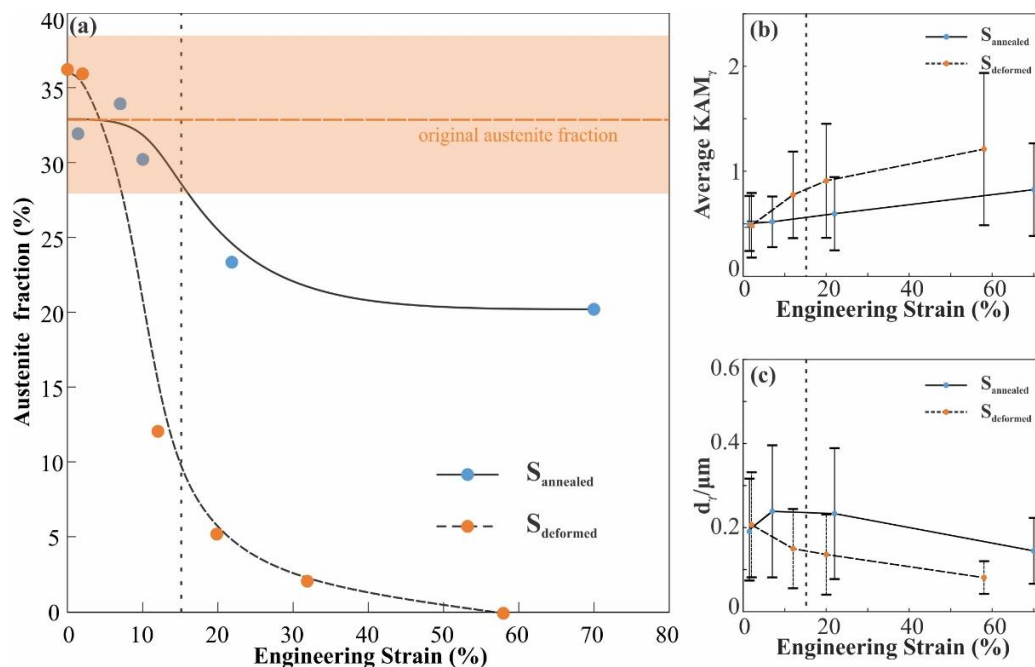**Figure 5.** An overview of (**a**) the austenite fraction changes, the (**b**) average KAM values, and (**c**) grain size of austenite as a function of strain-level, based on measurements shown in Fig. 3; In (**a**), the horizontal dashed line shows the average austenite volume fraction from multiple EBSD scans of $S_{original}$ samples, and the orange rectangle shows the standard deviation.

3.5. Mechanical effects

15

To systematically study how the dislocation density increase associated with the reversion process influences the mechanical properties, uniaxial tensile tests are carried out on $S_{original}$ and $S_{annealed}$. The deformation-induced microstructure changes of $S_{annealed}$ are confirmed by ECCI (Fig.6) and EBSD (Fig. 7b). The austenite grains in $S_{original}$ have granular shapes (Fig. 6a), with few straight features, suggesting the presence of stacking faults [39] (red arrows). As the sample is mechanically deformed,
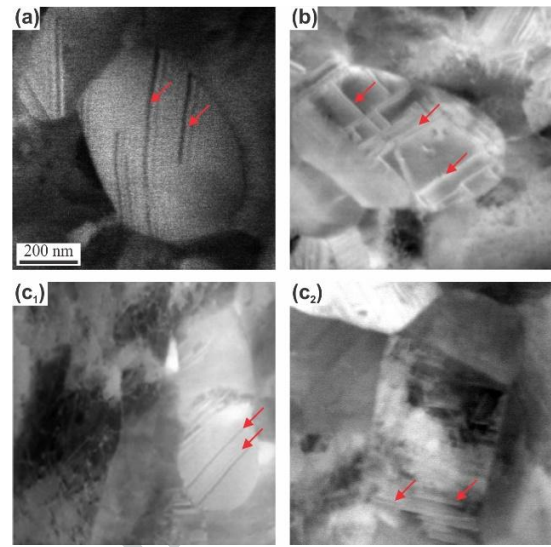

Figure 6. BSE images of austenite grains in **(a)** $S_{original}$, **(b)** $S_{deformed}$, and **(c$_{1-2}$)** $S_{annealed}$

most of the austenite transforms to martensite (Fig. 5a). The remaining austenite has a higher density of similar features, suggesting an increase in the stacking fault density on multiple {111} planes [40] (Fig. 6b, red arrow). After annealing, as discussed in the previous section, austenite grains are observed to have a range of stacking fault density (see Fig. 6c$_1$ vs. Fig. 6c$_2$). In most cases, we have observed only single variants of stacking faults. The EBSD analysis shows the same trend in phase transformation and defect evolution (Fig. 7b). The austenite fraction decreases from 36% to 12% after deformation and goes back to 34% after reversion annealing. KAM values in both austenite and martensite increase after deformation, and decrease after annealing.

Fig 7a shows the mechanical response of both $S_{original}$ and $S_{annealed}$, which are quantitatively compared in Fig. 7b. The $S_{annealed}$ shows a yield strength of 917 MPa, an ultimate tensile strength

16

of 1050 MPa, with 10% uniform elongation, and 24% total elongation. When compared with $S_{original}$, a slight increase in the ultimate tensile strength is observed, with no difference in the yield strengths. Testing samples with multiple deformation-annealing treatments (Fig. 7c, where uniform elongation (~8% strain) followed by an annealing treatment (at 600°C for 15 minutes) is referred to as one cycle), a steady change is observed. The work hardening curve of the same sample with cyclic treatment, revealing the increase in work hardening rate at the early stages of deformation (black arrow) as the cycle number increases. The yield strength (Fig. 7c insert) increases from 916 MPa (original) to 920 MPa (1 cycle) and then to 970 MPa (2 cycles). These hardening effects origins from the microstructure changes introduced by the deformation-annealing treatment (Fig. 3, Fig. 6).
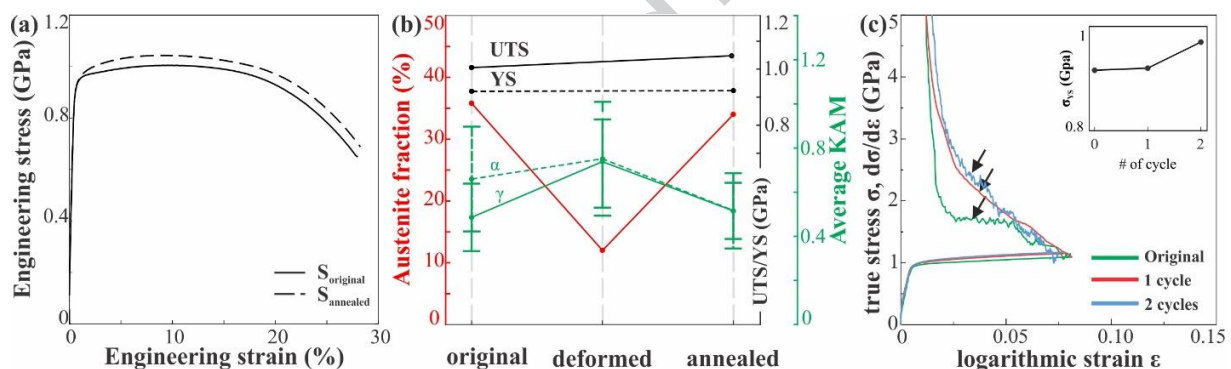

Figure 7. (a) The stress-strain curves of $S_{original}$ and $S_{annealed}$ (at a pre-strain level of 8%); **(b)** comparison of austenite fraction, UTS, YS, austenite grain size, and average KAM of $S_{original}$, $S_{deformed}$ (~ 8% deformation), and $S_{annealed}$ (~ 8% pre-strain); **(c)** the strain hardening curves of sample with different number of deformation-annealing-cycles and the yield strength changes (insert).

Recently, there has been an increasing interest to incorporate heat treatments to forming operations, either during forming or in-between forming steps [41,42]. Similarly, annealing treatments can be utilized to increase the accumulative ductility of TRIP-maraging steel, by reverting austenite that has transformed during the forming operation (benefitting from

17

martensite precipitates that resist tempering of the martensitic matrix) [20]. Figure 8 shows the

18

accumulative forming limit curve (FLC) and the fracture limit curve (FrLC) of TRIP-maraging steel. Methods that are used to define the diffuse necking strain and the fracture strain are explained in the supplementary material (Fig. S1 and Fig. S2). From FLC (Fig. 8a), the improvement in accumulative uniform strain is observed at both biaxial and uniaxial strain paths. At the uniaxial strain path, the original sample shows major strain 20%; the sample with one deformation-annealing cycle has accumulative major strain ~38% (doubled). Moreover, the
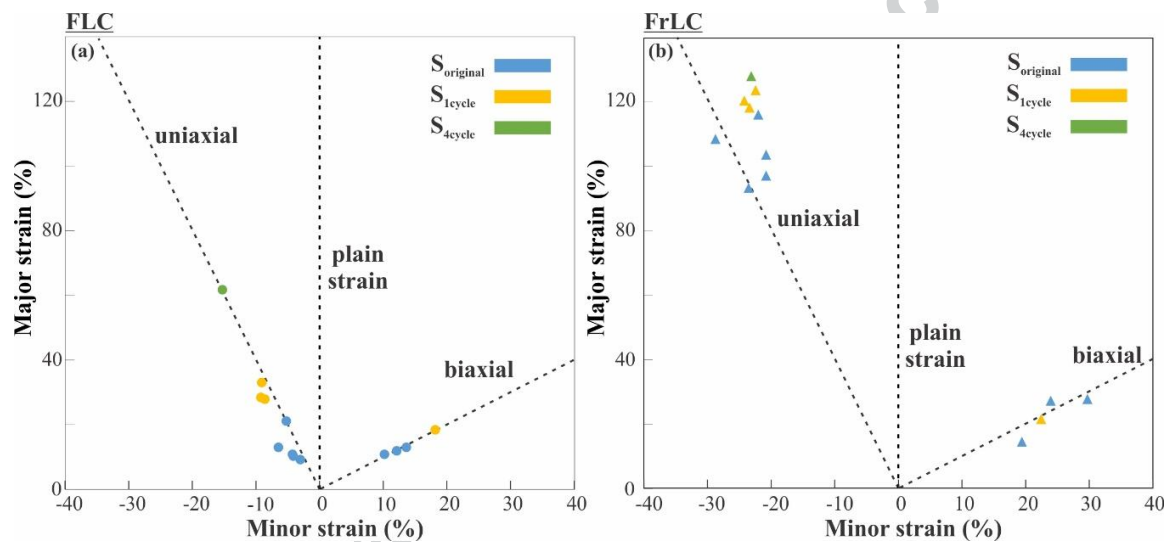
accumulative major strain reaches ~60% after the sample with four cycles of treatment. At the biaxial strain path, the accumulative uniform elongation with one deformation-annealing cycle is 1.5 times the original (from ~15% to ~20%). However, there are little improvements in FrLC for both strain path with extra deformation-annealing (Fig. 8b). For the uniaxial strain path, the fracture strain increases from ~105% to ~120% after one cycle, and then only increases to ~125% after four cycles of treatment. At the biaxial strain path, there is no difference between the original sample and the deformed-annealed sample.

19

Figure 8. Accumulative strains to failure plotted as classical **(a)** forming limit curve (FLC) and **(b)** fracture limit curve (FrLC) with 0, 1, and 4 cycles of deformation-annealing treatments.

The ductile fracture proceeds through damage nucleation and growth during plastic deformation [43]. The difference between FLC and FrLC (Fig. 8), i.e. presence of improvements in the former but not in the latter upon cyclic treatment, suggests an influence of damage accumulation. To systematically study how the damage evolution influences the mechanical properties, a post-mortem study of damage evolution as a function of local strain is carried out on the fractured $S_{original}$ and $S_{annealed}$ (Fig. 9).

At 0% local strain, the $S_{annealed}$ sample shows similar starting damage size, area fraction, and density as $S_{original}$ but with a larger standard deviation. The initial damage content typically arises from original processing steps (e.g. cold rolling). The small difference between the $S_{original}$ and $S_{annealed}$ shows that the annealing (without deformation) introduces little damage. At the uniform deformation region (0.2% to 18% local strain), the damage area fraction of the $S_{annealed}$ (~0.6%) is twice as the $S_{original}$ (~0.3%). There is no apparent increase in damage density (Fig. 9a), but the size of the damage incidence area fraction increases from ~0.1 μm^2 to 0.2 μm^2 (Fig. 9c). Since the $S_{annealed}$ has ~8% pre-strain, the accumulative deformation in $S_{annealed}$ is two times the accumulative deformation in $S_{original}$ at the same strain level. The increases in accumulative plastic strain cause the growth of crack and increase damage area fraction [21,43]. Interestingly, the increase in damage incident size does not cause an early failure of the material (Fig. 9). Instead, the $S_{annealed}$ keeps the crack size until local strain reaches ~70% (when all austenite is consumed according to Fig. 4). This is likely to be due to the mechanically induced martensitic transformation effect, which causes crack tip toughening [17]. When all the austenite phase

20

transformed, the $S_{annealed}$ has the same microstructure (mechanically induced martensite and martensite matrix) as the $S_{original}$ but with larger void size, which leads to earlier fracture [43].
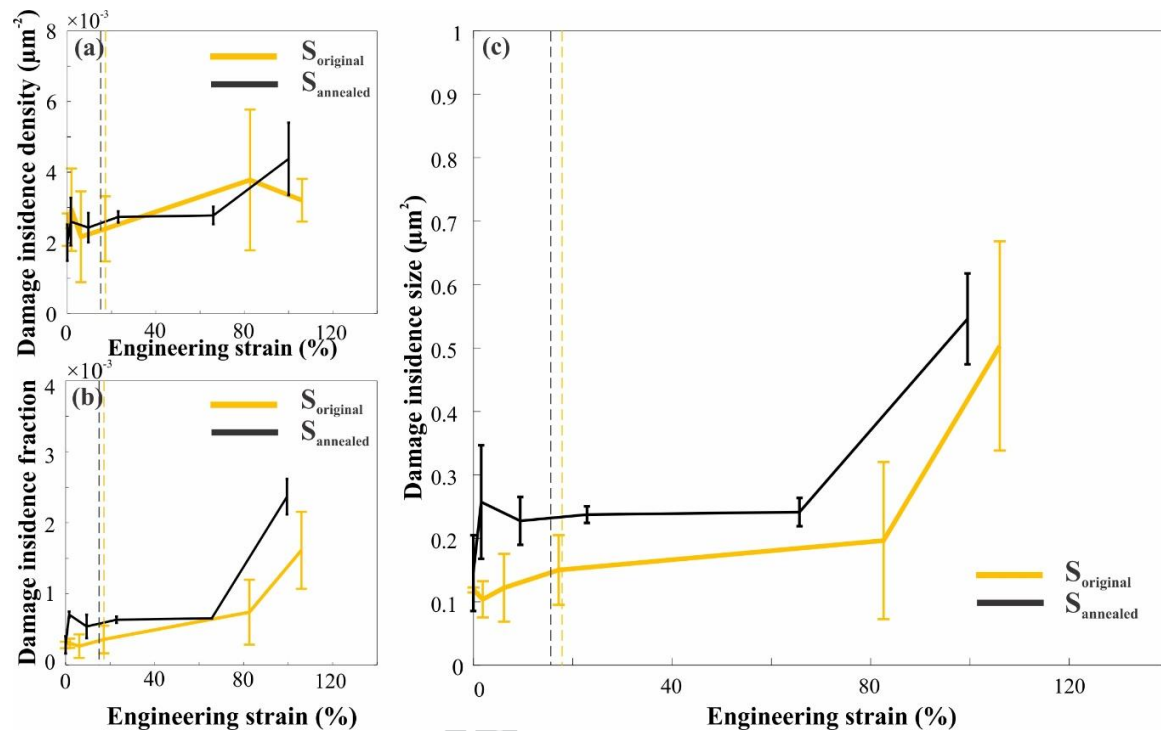

Figure 9. Quantification of damage evolution in $S_{original}$ and $S_{annealed}$ as a function of deformation: **(a)** damage incident density**; (b)** damage area fraction; **(c)** average damage incident size. The dashed line indicates the necking strain for each sample; the standard deviations represent the variations in different regions at the same local strain level.

4. Discussion

4.1 Austenite reversion mechanism

In plastically deformed TRIP-maraging steel martensitic constituents of different prior history coexist: deformed martensite matrix and mechanically induced martensite. In principle austenite reversion can take place in both, however, compositional and mechanical effects play an important role. In the original state ($S_{original}$), the austenite has a higher Mn concentration than the martensite matrix (Fig. 1b$_3$). The plastic deformation introduces displacive transformations ($\gamma \rightarrow$

21

α') and dislocation plasticity, which have negligible influences on the distribution of Mn. Thus, the mechanically induced martensite has a higher Mn concentration than the martensite matrix, which increases the thermodynamic driving force of the α'→ γ transformation [3] and decreases A_s temperature [44]. Moreover, the un-transformed austenite provides low energy boundaries for new austenite formation [11]. Due to these reasons, the nucleation of reversed austenite in mechanically induced martensite is preferred [20]. This also means that the reversed austenite is typically located in the same region as the original austenite (Fig. 3) [9,11]. In cases where the transformation of martensite to austenite is complete, the reversed austenite has the same grain size as the original austenite (Fig. 5c).

Austenite reversion can take place through displacive or diffusive α→γ transformations [1,11,45,46] (Fig. 2a). Transformation kinetics control the dominant reverse transformation mechanism as a function of the heating rate [1] (Fig. 2b). In carbon steels, extremely high heating rates (~50 K/s) are required to observe displacive austenite reversion [9]. The presented microstructure analyses, however, reveal a displacive-dominated reversion mechanism for the TRIP-maraging steel under the isothermal annealing conditions (moderate heating rates and short annealing time), based on three observations. First, the reversed austenite has a high dislocation and stacking fault density after transformation (Fig. 5b, Fig. 6). In displacive transformations, the microstructure of reversed austenite inherits the defects of the martensite phase [1,11]. The α'→ γ phase transformation introduces volume changes and grain rotation, which also causes residual stresses and increased defect density in the austenite phase [11]. Secondly, the reversed austenite has an acicular shape (Fig. 3a) and maintains a K-S relationship with the surrounding martensite phase

22

(Fig. 3). In displacive transformations, acicular shape and K-S relationship decrease nucleation energy [2,8,32]. Thirdly, the neighboring martensite has high defect density (Fig. 3), which is to compensate for the volume change and grain rotation during displacive reversion [8,11]. This difference in the behavior of the TRIP-maraging steel compared to carbon steels can be related to the diffusion of the corresponding austenite stabilizing element. Compared to the relatively higher diffusion coefficient of the interstitial carbon in the latter, the main austenite stabilizer is the substitutional Mn in the TRIP-maraging steel, which has lower diffusivity [3].

4.2 Pre-strain effect on reverse transformation kinetics

Next, we discuss the pre-straining effects on the reverse transformation of mechanically induced martensite. Results presented here reveal that at a low pre-strain level, the austenite volume fraction can return to its original value (Fig. 5). Further increases in the applied pre-strain levels lead to the development of increasing defect density in the reverted austenite, and the austenite volume fraction does not return to its original value. For example, for the highest pre-strain level, the lowest austenite fraction is achieved upon reversion, resulting in austenite grains with small grain size and acicular shape (Fig. 7).

The TRIP effect of the metastable austenite provides the primary plasticity mechanism in these alloys (Fig. 7b) [5,21], whereas the martensite matrix and the mechanically induced martensite show relatively smaller plasticity contributions at low strain levels [47]. At higher pre-strain levels, the mechanically induced martensite also exhibits dislocation plasticity (Fig. 7b) [47]. Increased dislocation density can decrease boundary mobility and grain growth rates [11]. However, as observed here (Fig. 3b, 3c), it can also provide increased density of nucleation sites for austenite
23

reversion [12,48], promoting further austenite reversion by the formation of multiple nuclei. On the other hand, the hardening of the martensite matrix (Fig. 3a$_4$, Fig. 7) increases the elastic strain energy penalty of the shear transformation [49]. As a result of these effects, although the displacive transformation is directly followed by a recovery process (Fig. 2, peak3) [1], high dislocation density austenite grains are formed as the pre-strain level increases, and the dislocation structure is maintained (Fig. 3, Fig. 6). Further increase in the pre-strain level leads to only the partial reversion of the austenite, where kinetical effects of the increased defect density on boundary mobility apparently starts to govern the transformation.

4.3 Microstructure evolution and the influence in mechanical properties

As discussed above, the microstructure development during annealing depends highly on the plastic deformation during pre-straining. Focusing on the uniform pre-strain (~8%), where the $S_{annealed}$ has the same volume fracture as the $S_{original}$, resulting mechanical effects can be discussed. The $S_{annealed}$ exhibits similar ductility, but a slight increase of yield strength and ultimate strength.

The mechanically induced transformation contributes to ductility by increasing strain hardening capacity [21] and damage resistance (Fig. 9) [17]. During austenite reversion ($S_{deformed}$ to $S_{annealed}$), the shear transformation from mechanically induced martensite to austenite is preferred instead of random nucleation at martensite boundaries, because of the Mn enrichment [20]. When the reversion is complete after annealing, the reversed austenite grains inherit the original austenite boundaries (Fig. 3b, 3c), the grain morphology and size (which highly influence the austenite stability [16,50]) remain the same (Fig. 4, Fig. 7), as well as the volume fraction of austenite. Thus, similar ductility is observed (Fig. 7) [16]. Although there is dislocation accumulation in austenite
24

grains during transformation (Fig. 3, 6, 7) which can cause mechanical stabilization [18], the reversed austenite phase in the $S_{annealed}$ remains metastable, and exhibits mechanically induced transformation. The accumulation of dislocations and stacking faults (Fig. 5, Fig. 6c) in the austenite increases the work hardening rate [18] and yield strength [13,51] (Fig. 7). On the other hand, damage in $S_{annealed}$ is arising both from pre-straining, and the deformation during testing (Fig. 9). The accumulated damages influence mainly the post-necking behavior: upon consumption of all the austenite, the work hardening rate decreases significantly (Fig. 5) and the fracture takes place earlier.

There are other microstructural changes during the displacive austenite reversion [52], which are not discussed here. The reversed austenite formed within the mechanically induced martensite does not necessarily inherit the original grain morphology given the possibility of multi-site nucleation (Fig. 3), which causes a decrease in grain size. In austenitic stainless steel, mechanically induced martensitic transformation combined with thermally induced reverse transformation is an effective method of grain refinement and strengthening [53]. Moreover, the reversed austenite has 24 variants [2,52,54], which means that the deformation-annealing treatment changes the austenite orientation distribution.

5. Conclusions

In summary, the austenite in the TRIP-maraging steel exhibits displacive phase transformation characteristics during reversion treatment following mechanically induced transformation. The newly formed austenite has similar grain size, morphology, and phase volume fraction, which enables the $S_{annealed}$ to maintain the ductility of the original TRIP-maraging steel. Because of the

25

displacive transformation, the reversed austenite has a higher dislocation density than the original sample, which creates increases in the yield strength, ultimate strength, and work hardening rate. The pre-strain level profoundly influences the defect density in the mechanically induced martensite and changes displacive transformation driving force and kinetics. Full austenite reversion is observed only when the deformation level is low. From an engineering perspective, the reversion process provides opportunities to increase the accumulative ductility of metastability assisted alloys, improving their forming limits (although fracture limits may remain unchanged).

Data availability

The raw/processed data required to reproduce these findings cannot be shared at this time as the data also forms part of an ongoing study.

Reference

1   K. Tomimura, S. Takaki, and Y. Tokunaga: *ISIJ Int.*, 1991, vol. 31, pp. 1431–7.

2   N. Nakada, T. Tsuchiyama, S. Takaki, and S. Hashizume: *ISIJ Int.*, 2007, vol. 47, pp. 1527–32.

3   D. Raabe, S. Sandlöbes, J. Millán, D. Ponge, H. Assadi, M. Herbig, and P.-P.P. Choi: *Acta Mater.*, 2013, vol. 61, pp. 6132–52.

4   R.D.K. Misra, S. Nayak, S.A. Mali, J.S. Shah, M.C. Somani, and L.P. Karjalainen: *Metall. Mater. Trans. A*, 2009, vol. 40, pp. 2498–509.

5   M.M. Wang, C.C. Tasan, D. Ponge, and D. Raabe: *Acta Mater.*, 2016, vol. 111, pp. 262–72.

6   J.T.T. Benzing, A. Kwiatkowski da Silva, L. Morsdorf, J. Bentley, D. Ponge, A. Dutta, J. Han, J.R.R. McBride, B. Van Leer, B. Gault, D. Raabe, and J.E.E. Wittig: *Acta Mater.*, 2019, vol. 166, pp. 512–30.

7   B. Hu, H. Luo, F. Yang, and H. Dong: *J. Mater. Sci. Technol.*, 2017, vol. 33, pp. 1457–64.

8   K. Bhattacharya: *Microstructure of Martensite: Why It Forms and How It Gives Rise to the Shape-Memory Effect*, vol. 41, Oxford University Press, 2004.

9   N. Nakada, T. Tsuchiyama, S. Takaki, D. Ponge, and D. Raabe: *ISIJ Int.*, 2013, vol. 53, pp. 2275–7.

26

10   J. Han, S.J. Lee, J.G. Jung, and Y.K. Lee: *Acta Mater.*, 2014, vol. 78, pp. 369–77.

11   N. Nakada: *Mater. Lett.*, 2017, vol. 187, pp. 166–9.

12   B.B. He and M.X. Huang: *Metall. Mater. Trans. A Phys. Metall. Mater. Sci.*, 2016, vol. 47, pp. 3346–53.

13   B.B. He, M. Wang, and M.X. Huang: *Metall. Mater. Trans. A*, 2019, vol. 50, pp. 2971–7.

14   J. Zhu, R. Ding, J. He, Z. Yang, C. Zhang, and H. Chen: *Scr. Mater.*, 2017, vol. 136, pp. 6–10.

15   B. Hu, B. He, G. Cheng, H. Yen, M. Huang, and H. Luo: *Acta Mater.*, 2019, vol. 174, pp. 131–41.

16   M.-M. Wang, C.C. Tasan, D. Ponge, A. Kostka, and D. Raabe: *Acta Mater.*, 2014, vol. 79, pp. 268–81.

17   M. Koyama, Z. Zhang, M. Wang, D. Ponge, D. Raabe, K. Tsuzaki, H. Noguchi, and C.C. Tasan: *Science*, 2017, vol. 355, pp. 1055–7.

18   A. Alaei, H. Jafarian, and A.R. Eivani: *Mater. Sci. Eng. A*, 2016, vol. 676, pp. 342–50.

19   S. Wei, M. Jiang, and C.C.C.C. Tasan: *Metall. Mater. Trans. A*, 2019, vol. 50, pp. 3985–91.

20   M. Wang, M. Jiang, and C.C. Tasan: *Scr. Mater.*, 2020, vol. 179, pp. 75–9.

21   M.M. Wang, C.C. Tasan, D. Ponge, A.C. Dippel, and D. Raabe: *Acta Mater.*, 2015, vol. 85, pp. 216–28.

22   T. O'Haver: *Univ. Maryl. Coll. Park. Coll. Park. MD, accessed Jan*, 1997, vol. 14, p. 2018.

23   C.C. Roth and D. Mohr: *Int. J. Plast.*, 2016, vol. 79, pp. 328–54.

24   C.G. van Essen, E.M. Schulson, and R.H. Donaghay: *Nature*, 1970, vol. 225, pp. 847–8.

25   C.A. Schneider, W.S. Rasband, and K.W. Eliceiri: *Nat. Methods*, 2012, vol. 9, pp. 671–5.

26   W.A. Johnsson and R.F. Mehl: *Trans. Am. Inst. Min. Met. Eng.*, 1940, vol. 135, pp. 416–42.

27   E.J. Mittemeijer: *J. Mater. Sci.*, 1992, vol. 27, pp. 3977–87.

28   Z. Guo, W. Sha, and D. Li: *Mater. Sci. Eng. A*, 2004, vol. 373, pp. 10–20.

29   M. Wang: *PhD thesis*.

30   M.C. Somani, P. Juntunen, L.P. Karjalainen, R.D.K. Misra, and A. Kyröläinen: *Metall. Mater. Trans. A*, 2009, vol. 40, pp. 729–44.

31   V.N. Khachin: *Martensitic Transformation*, Elsevier, 1978.

32   P.M. Kelly, A. Jostsons, and R.G. Blake: *Acta Metall. Mater.*, 1990, vol. 38, pp. 1075–81.

33   N. Nakada, T. Tsuchiyama, S. Takaki, and N. Miyano: *ISIJ Int.*, 2011, vol. 51, pp. 299–304.

34   S. Zaefferer and N.N. Elhami: *Acta Mater.*, 2014, vol. 75, pp. 20–50.

35   F. Roters, P. Eisenlohr, L. Hantcherli, D.D. Tjahjanto, T.R. Bieler, and D. Raabe: *Acta Mater.*, 2010, vol. 58, pp. 1152–211.

36   X.D. Wang, B.X. Huang, Y.H. Rong, and L. Wang: *Mater. Sci. Eng. A*, 2006, vol. 438–440, pp. 300–5.

37   M. Naghizadeh and H. Mirzadeh: *Steel Res. Int.*, 2019, vol. 90, pp. 1–9.

38   S. Chatterjee, H.-S.S. Wang, J.R. Yang, and H.K.D.H.D.H. Bhadeshia: *Mater. Sci. Technol.*, 2006, vol. 22, pp. 641–4.

39   I. Gutierrez-Urrutia, S. Zaefferer, and D. Raabe: *Jom*, 2013, vol. 65, pp. 1229–36.

40   A. Weidner, S. Martin, V. Klemm, U. Martin, and H. Biermann: *Scr. Mater.*, 2011, vol. 64, pp. 513–6.

27

41   Z. Liu: *Int. J. Adv. Manuf. Technol.*, DOI:10.1007/s00170-018-2470-3.

42   K. Lange: *McGraw-Hill B. Company, 1985,* 1985, p. 1216.

43   P.F. Thomason: *Pergamon Press*, 1990, p. 219.

44   E. De Moor, D.K. Matlock, J.G. Speera, and M.J. Merwin: *Scr. Mater.*, 2011, vol. 64, pp. 185–8.

45   R.W. Balluffi, S.M. Allen, and W.C. Carter: *Kinetics of Materials*, John Wiley & Sons, 2005.

46   J. Han and Y.-K. Lee: *Acta Mater.*, 2014, vol. 67, pp. 354–61.

47   M.I. Latypov, S. Shin, B.C. De Cooman, and H.S. Kim: *Acta Mater.*, 2016, vol. 108, pp. 219–28.

48   K.E. Easterling and A.R. Thölén: *Acta Metall.*, 1976, vol. 24, pp. 333–41.

49   H.C. Fieldler, B.L. Avergach, and M. Cohen: *Trans. ASM*, 1995, vol. 47, pp. 267–90.

50   S.J. Lee, S.J. Lee, and B.C. De Cooman: *Mater. Sci. Technol. Conf. Exhib. 2011, MS T'11*, 2011, vol. 1, pp. 545–51.

51   T.J. Koppenaal and E. Gold: *Metall. Trans.*, 1972, vol. 3, pp. 2965–72.

52   K. Bhattacharya, S. Conti, G. Zanzotto, and J. Zimmer: *Nature*, 2004, vol. 428, pp. 55–9.

53   F. Forouzan, A. Najafizadeh, A. Kermanpur, A. Hedayati, and R. Surkialiabad: *Mater. Sci. Eng. A*, 2010, vol. 527, pp. 7334–9.

54   H. Kessler and W. Pitsch: *Acta Metall.*, 1965, vol. 13, pp. 871–4.

28